Guided Mode Evolution and Ionization Injection in Meter-Scale Multi-GeV Laser Wakefield Accelerators

J. E. Shrock,[1] E. Rockafellow,[1] B. Miao,[1] M. Le,[1] R. C. Hollinger,[2] S. Wang,[2] A. J. Gonsalves,[3] A. Picksley,[3] J. J. Rocca,[2,4] and H. M. Milchberg[1,5]

[1]*Institute for Research in Electronics and Applied Physics and Department of Physics, University of Maryland, College Park, Maryland 20742, USA*

[2]*Department of Electrical and Computer Engineering, Colorado State University, Fort Collins, Colorado 80523, USA*

[3]*Lawrence Berkeley National Laboratory, Berkeley, California 94720, USA*

[4]*Department of Physics, Colorado State University, Fort Collins, Colorado 80523, USA*

[5]*Department of Electrical and Computer Engineering, University of Maryland, College Park, Maryland 20742, USA*

(Received 13 September 2023; revised 19 May 2024; accepted 18 June 2024; published 26 July 2024)

We show that multi-GeV laser wakefield electron accelerators in meter-scale, low density hydrodynamic plasma waveguides operate in a new nonlinear propagation regime dominated by sustained beating of lowest order modes of the ponderomotively modified channel; this occurs whether or not the injected pulse is linearly matched to the guide. For a continuously doped gas jet, this emergent mode beating effect leads to axially modulated enhancement of ionization injection and a multi-GeV energy spectrum of multiple quasimonoenergetic peaks; the same process in a locally doped jet produces single multi-GeV peaks with $<10\%$ energy spread. A three-stage model of drive laser pulse evolution and ionization injection characterizes the beating effect and explains our experimental results.

DOI: 10.1103/PhysRevLett.133.045002

Laser-driven plasma wakefields [1,2] have accelerating gradients $\sim$1000 times larger than those in linear rf accelerators, enabling the production of multi-GeV electron bunches in centimeters [3–6]. In general, optical guiding is needed to keep the intensity of the driving laser high and extend the acceleration length. While relativistic self-guiding has resulted in $\sim$2 GeV electron bunches, it demands petawatt-scale laser powers [3,4]. More laser-energy-efficient and controllable acceleration of electrons can be achieved by using plasma waveguides [5–22].

Recently, we demonstrated laser wakefield acceleration (LWFA) of electrons to 5 GeV in a 20 cm plasma waveguide using $<$300 TW of laser power [6]. In our scheme, which employs hydrodynamic plasma waveguides [7,8] generated in Bessel-beam-heated meter-scale gas jets [6,22], the laser pulse undergoes "self-waveguiding" [20,21], while simultaneously driving the plasma wake responsible for electron acceleration. First, a zeroth order ultrashort pulse Bessel beam with a 50 cm long focus ionizes and heats (by optical-field ionization [12–22]) a 20 cm long hydrogen $95\%/5\%-H_2/N_2$ gas sheet. The explosive hydrodynamic response leaves a $\sim 10\times$ reduced gas density on axis surrounded by an expanding cylindrical shock shell of enhanced density measured by two-color interferometry [20]. When end-injected by a high intensity laser pulse, the core and inside walls of this "prepared index structure" are ionized by the very early leading edge of the injected pulse, forming an on-the-fly plasma waveguide that confines most of the pulse. The accelerated electrons are injected into the wake by ionization injection [23–26] of N^{5+}.

In this Letter, we present experiments and simulations demonstrating that laser intensity oscillations from a general mode beating effect—*active whether or not the injected laser is linearly mode matched to the guide*—are responsible for periodically enhanced ionization injection, giving rise to characteristic multipeaked electron spectra at multi-GeV energies. A three-stage model of intense laser propagation explains our results. Insight from this model then motivates an experiment showing that mode beating at an axially localized dopant region produces quasimonoenergetic multi-GeV electron bunches with energy spread $<10\%$ and mrad divergence. The mode-beating-induced injection effect described in this work is new and emerges from the use of narrow, low density meter-scale plasma waveguides.

Figure 1 presents results from a representative WarpX particle-in-cell (PIC) simulation [27] for the parameters of our experiments, using a $95\%/5\%-H_2/N_2$ gas mix. The figure shows pulse evolution and electron acceleration for a LWFA drive pulse (blue curve: $a_{0i} = 2.0$, $\tau_{\mathrm{FWHM}} = 41$ fs, $w_0 = 30$ μm Gaussian pulse) injected into a 20 cm waveguide with on-axis plasma density $N_{e0} = 2.0 \times 10^{17}$ cm^{-3}, where $w_{ch} = 20$ μm is the e^{-2} intensity radius of the lowest order self-waveguided mode of the structure shown in Fig. 1(d) and computed using our leaky mode solver [9,20,28,29]. The injected pulse is therefore mode-mismatched. Figures 1(a) and 1(b) plot the peak normalized vector potential and

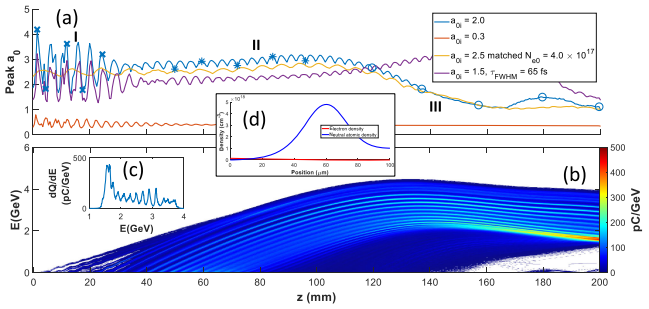

FIG. 1. WarpX [27] particle-in-cell simulations of drive pulse evolution in a waveguide formed from the prepared index structure [20] shown in the central inset, with $w_{ch} = 20$ μm. Gas composition is $95\%/5\%-H_2/N_2$ and the simulation xyz grid is $256 \times 256 \times 4096$ (256 μm × 256 μm × 204.8 μm). (a) Peak laser field a_0 vs propagation distance for (i) mismatched input field $a_{0i} = 2.0$, $w_0 = 30$ μm, $\tau_{\mathrm{FWHM}} = 41$ fs, $N_{e0} = 2.0 \times 10^{17}$ cm^{-3} (blue curve); (ii) mismatched input field $a_{0i} = 1.5$, $w_0 = 30$ μm, $\tau_{\mathrm{FWHM}} = 65$ fs, $N_{e0} = 2.0 \times 10^{17}$ cm^{-3} (purple curve); (iii) mismatched $a_{0i} = 0.3$, $w_0 = 30$ μm, $\tau_{\mathrm{FWHM}} = 41$ fs, $N_{e0} = 2.0 \times 10^{17}$ cm^{-3} (orange curve); and (iv) matched $a_{0i} = 2.5$, $w_0 = 30$ μm, $\tau_{\mathrm{FWHM}} = 41$ fs, $w_{ch} = 30$ μm, $N_{e0} = 4.0 \times 10^{17}$ cm^{-3} (gold curve, Gaussian input pulse, parabolic channel). Labels I, II, and III denote the three characteristic propagation stages. Labels (×), (∗), and (o) denote the locations of the frames displayed in Figs. 2(a)–2(c). (b) Electron spectrum vs propagation distance corresponding to the blue curve of (a). (c) Final integrated spectrum. (d) Prepared index structure measured by two-color interferometry [20] and fitted to even polynomial × exponential.

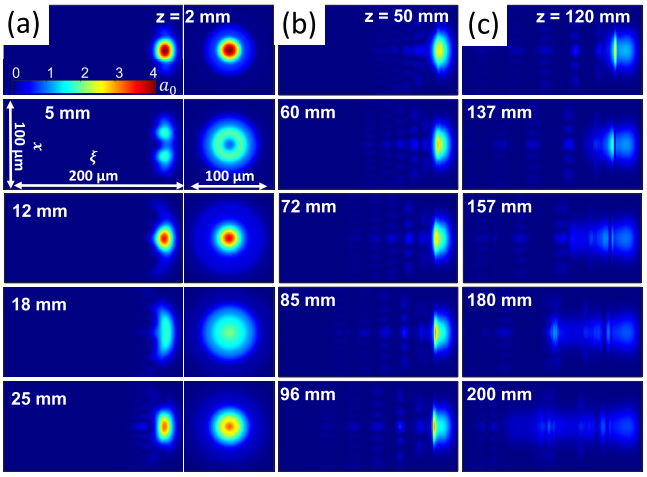

FIG. 2. Evolution of LWFA drive pulse corresponding to the blue curve in Fig. 1(a). Column (a) for stage I, plots $x\xi$ slices of the field magnitude a_0 on the left and the ξ-integrated mode on the right, where $\xi = z - ct$ is the space coordinate in the moving computation frame. Longitudinal positions denoted on the frames are marked by the blue crosses in Fig. 1(a). Column (b), for stage II, plots $x\xi$ slices of a_0 for the longitudinal positions marked by the blue stars. Column (c), for stage III, plots $x\xi$ slices of a_0 for the longitudinal positions marked by the open circles in Fig. 1(a). All slices and profiles are normalized to the maximum at $z = 2$ mm.

electron energy spectrum vs z. The spectrum shows a striated energy structure caused by periodic ionization injection of electrons from N^{5+}; comparing panels reveals that individual striations are correlated with a_0 oscillations. With increasing z, the striations bend over as dephasing begins, and by $z = 20$ cm the final spectrum of Fig. 1(c) shows that multiple quasimonoenergetic peaks remain. The characteristic features of these plots are observed for a wide variety of conditions [28]. In pure H_2, pulse evolution is similar to that in Fig. 1(a), but with no electron injection and acceleration [28], in agreement with no experiments observing acceleration in pure H_2 waveguides.

We identify three stages of pulse evolution as marked on the blue curve in Fig. 1(a): (I) large amplitude intensity oscillations during early propagation, which quickly transition to (II) sustained oscillations at lower amplitude, followed by (III) intensity decline and cessation of regular oscillations. Periodic ionization injection and the striated bunch energy structure occur during stages I and II; the degree of dephasing between the electron bunches and the plasma wake during stage III determines if this structure is preserved.

The oscillations in stages I and II suggest beating between different plasma waveguide modes. Although the modes of hydrodynamic plasma waveguides are strictly quasibound or "leaky" [9,29], an excellent approximation for low order modes of symmetric guides [9,28] is the spectrum of bound mode wave numbers of a parabolic plasma profile, $\beta_{pm} = k_0[1 - N_{e0}/2N_{cr} - 2(2p + m + 1)/k_0^2 w_{ch}^2]$, where (p, m) identifies the radial and azimuthal indices, N_{cr} is the plasma critical density, $w_{ch} = (\pi r_e \Delta N_e)^{-1/2}$, $\Delta N_e = N_e(w_{ch}) - N_e(0)$, $r_e = e^2/mc^2$ is the classical electron radius, and $k_0 = 2\pi/\lambda_0$ is the vacuum wave number [9,28]. The spatial beat period for two interfering modes is $\Lambda = 2\pi/|\beta_{p'm'} - \beta_{pm}|$. Mode beating between the (0,0) and (1,0) plasma waveguide modes, due to linear mismatch between the drive pulse and waveguide, has already been studied in Ref. [20]. Each mode has a characteristic $1/e$ propagation decay length, $L_{1/e}$, which is longest for the (0,0) mode and decreases for higher order modes [9]. In the blue curve in Fig. 1(a), the oscillation period in stage I is $\Lambda \sim 4.4$ mm, corresponding to beating dominantly between the (0,0) and (1,0) modes [28], with higher order modes contributing higher frequency interference. Despite the $L_{1/e} \sim 7$ m and ∼1 m decay lengths of the (0,0) and (1,0) modes, the stage I beating quickly transitions to the lower amplitude oscillations of stage II.

To obtain further insight, we examine Fig. 2. Figures 2(a)–2(c) show the laser field magnitude a_0 in the xz plane; the right column in 2(a) shows the field profile in the transverse (xy) plane integrated over the pulse envelope. The panels are ordered vertically by the z locations marked on the blue curve in Fig. 1(a). The large

amplitude oscillations of stage I manifest in Fig. 2(a) as mode shape and size oscillations corresponding to the (0,0) and (1,0) modes. By $z = 25$ mm, as stage I beating is fading, a small intensity tail has split off, lagging the main pulse. By $z = 50$ mm, (stage II), a sequence of evenly spaced high order pulselets has increasingly separated from the main pulse, with the highest order modes the most delayed. This is understood as group velocity walk-off of higher order modes according to [9,20] $v_{g,pm} = (\partial\beta_{pm}/\partial\omega)^{-1} = c[1 - N_{e0}/2N_{cr} - 2(2p + m + 1)/k_0^2 w_{ch}^2]$. However, as seen in the panels in Fig. 2(b) and the associated propagation movies in [28], the (1,0) structure remains tethered to the (0,0) structure by a long tail, sustaining the beating until $z > \sim 110$ mm, whereupon the stage II oscillations decay as the wake weakens. Owing to the strong w_{ch} dependence of $v_{g,pm}$, this effect may be less observable in capillary waveguides, which typically have $w_{ch} > 50$ μm.

Further examination of Fig. 1(a) explains the propagation physics. A low intensity, *mode-mismatched* injected pulse with $a_{0i} = 0.3$ and $w_0 = 30$ μm (orange curve), reproduces the stage I mode beating of the blue curve; here the beating terminates with complete walk-off of the (1,0) mode. For a higher intensity *mode-matched* Gaussian pulse in a parabolic channel [$a_{0i} = 2.5$, $\tau_{\mathrm{FWHM}} = 35$ fs, $w_0 = 30$ μm, $w_{ch} = 30$ μm, and $N_{e0} = 4.0 \times 10^{17}$ cm^{-3} (gold curve)], the stage I oscillations of the blue curve are absent, replaced by regular low amplitude oscillations (seen in [30–33]) extending through $z > 110$ mm (the mode-matched case of $a_0 = 2.0$ and $N_{e0} = 2.0 \times 10^{17}$ cm^{-3} yields little injection and acceleration). These oscillations are similar to the blue curve stage II oscillations, and both can be understood as beating of the (0,0) and (1,0) modes of a *ponderomotively modified channel*, where $w_{ch}^{\mathrm{blue}} = 18$ μm (in stage II) and $w_{ch}^{\mathrm{gold}} = 24$ μm are determined from the simulations [28]. Each is less than its corresponding unperturbed channel mode radius $w_{ch,0}$ (20 μm and 30 μm, respectively).

The sustained beating of (0,0) and (1,0) modes appears to be a general feature of $a_0 > 1$ laser pulse propagation in a plasma waveguide, *whether or not the injected pulse is linearly mode-matched to the guide*. As simulation movies show [28], pulse front erosion and red shifting from wake excitation, along with self-steepening at the back of the pulse, continuously feed energy from the front of the pulse, where $w_{ch} = w_{ch,0}$, to the cavitated region of the pulse centroid, where $w_{ch} < w_{ch,0}$. This effective mismatch couples to the (0,0) and (1,0) modes, generating a beat period $\Lambda = 2\pi/|\beta_{10} - \beta_{00}| = \pi^2 \lambda_0 (w_{ch}/\lambda_0)^2$. For the specific cases of Fig. 1(a), $w_{ch} = w_{ch}^{\mathrm{blue}}$ (in stage II) gives $\Lambda_{\mathrm{blue}} = 4.0$ mm and $w_{ch} = w_{ch}^{\mathrm{gold}}$ gives $\Lambda_{\mathrm{gold}} = 7.1$ mm. These are in good agreement with the oscillation periods from the simulations in Fig. 1(a).

This beating results in periodic axial modulations of the pulse envelope, with the peak a_0 moving back and forth in the pulse frame [28]. High-resolution PIC simulations (see Appendix B) show that injection is enhanced during the phase of beating when the local peak in a_0 is closest to the minimum of the wake potential. While some injection occurs during stage I, the large amplitude beating induces significant distortion of the wake and loss of trapped electrons. By $z > 80$ mm, ionization injection in stage II ceases owing to pulse self-steepening and etching [28]. By stage III [Fig. 2(c)], the pulse has dispersed and broken up from red shifting and pulse stretching. Here, depletion-induced dephasing [6,34] results in a reduction of maximum accelerated electron energy for $z > 140$ mm, but the striated energy structure is preserved because the pulse is too weak to disrupt the wakefield structure. For higher laser intensity and/or plasma density, we observe pulse breakup earlier in propagation, leading to wakefield distortion and loss of the striated energy structure [28]. A decrease in drive pulse energy (due, for example, to mismatched coupling) may also cause an earlier onset of depletion and loss of striations in the energy spectrum [28].

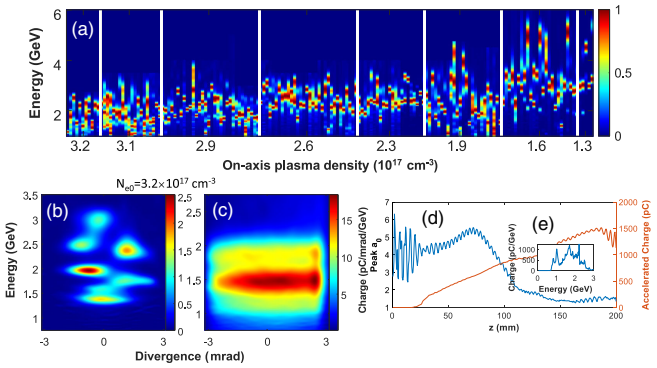

FIG. 3. (a) Angularly integrated electron spectra varying plasma density (P1 was 11 J, $\tau_{\mathrm{FWHM}} = 65$ fs, $w_0 = 30$ μm and $a_0 \sim 2.0$), showing multipeak spectra ranging from >1 GeV to <6 GeV. Here, a 95%/5%−H_2/N_2 gas mix was injected by all six valves along the gas jet. Multiple shots were taken in each density bin, with an increase in accelerated electron energy as density drops. Each spectrum is normalized to its peak. (b) Example of multipeak spectrum with $a_{0i} = 2$ and $N_{e0} = 3.2 \times 10^{17}$ cm^{-3}. (c) Example of "washed out" spectrum for higher intensity and waveguide density: $a_{0i} = 2.5$ and $N_{e0} = 3.2 \times 10^{17}$ cm^{-3}. (d),(e) Results of PIC simulation for conditions of (c) showing early onset of depletion. Charge is for >1 GeV.

The three-stage picture is well-matched to our self-waveguided LWFA experiments at the ALEPH laser system [35] at Colorado State University. Details of the experimental setup are presented in Appendix A. We used three gas flow configurations: pure H_2, a dopant gas mix (95%/5%H_2/N_2), or pure H_2 with added localized injection of the dopant gas mix.

Figure 3(a) is a plot of angle-integrated electron bunch spectra vs plasma waveguide central density N_{e0} for the case of the dopant gas mix supplied to all six jet valves.

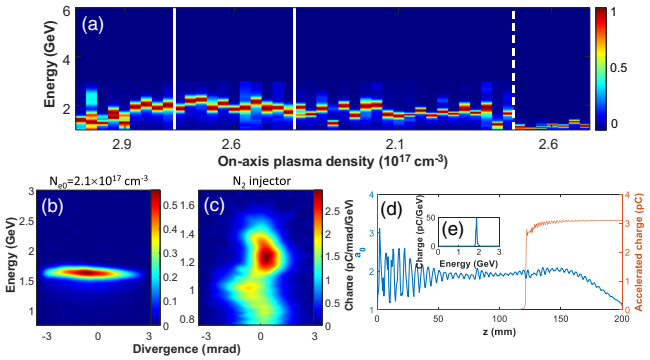

FIG. 4. (a) Angularly integrated electron spectra from multiple shots in each density bin, showing mostly single quasimonoenergetic peaks <2.5 GeV. Here, $a_{0i} = 2.0$, and pure H_2 was injected by all six valves along the gas jet, with a 95%/5%−H_2/N_2 dopant gas injector either at $z = 10$ cm (spectra to the left of the dashed white line) or $z = 14$ cm (spectra to the right of the dashed white line, where the waveguide central plasma density was fixed at $N_{e0} = 2.6 \times 10^{17}$ cm^{-3}). Each spectrum is normalized to its peak. (b) Example of quasimonoenergetic spectrum with $a_{0i} = 2.0$ and $N_{e0} = 2.1 \times 10^{17}$ cm^{-3} (localized dopant at $z = 10$ cm). (c) Example of spectrum resulting from pure N_2 injector at $z = 14$ cm, showing continuous injection. (d),(e) Results of WarpX simulation for $a_{0i} = 1.5$ and $N_{e0} = 2.1 \times 10^{17}$ cm^{-3} with localized dopant at $z = 10$ cm. Charge is for >1 GeV.

Here, P1 (11 J, $\tau_{\mathrm{FWHM}} = 65$ fs, $w_0 = 30$ μm and $a_{0i} \sim 2.0$) was injected at 2.5 ns delay into the prepared index structure generated by P2 (0.5 J, $\tau_{\mathrm{FWHM}} = 75$ fs). The spectra vary shot to shot, under nominally similar conditions, due to injected laser pointing and energy fluctuations [6,28], but the majority of the spectra [such as Fig. 3(b)] are multipeaked spectra consistent with the simulations of Fig. 1 for the case of dopant gas all along the waveguide. The distribution of the peaks shifts to higher energies with decreasing plasma density, as expected [6]. For higher P1 intensity (15 J, $\tau_{\mathrm{FWHM}} = 45$ fs, $w_0 = 30$ μm, and $a_0 \sim 2.6$), the multipeak spectrum gives way to a broad, high charge and lower energy peak as illustrated by Fig. 3(c). The simulation of Fig. 3(d) for these conditions shows that higher laser intensity causes earlier onset of depletion-induced dephasing (stage III of pulse propagation), resulting in earlier rollover of the spectrum [compared to Fig. 1(b)], suppressing the lower energy striations and washing out the higher energy striations into a broad peak.

To generate a quasimonoenergetic spectrum, these results suggest employing the intensity oscillations as an injector over a localized region of dopant gas, an approach also used in capillary discharge waveguides [36,37]. Our gas jet design ([22], Appendix A) provides this capability via axially localized dopant gas inlets. Figure 4(a) is a plot of angle-integrated electron bunch spectra vs plasma waveguide central density N_{e0} for the case of pure H_2 supplied to all six jet valves, and the dopant gas mix supplied through an injector either at $z = 10$ cm (left side of white dashed line) or at $z = 14$ cm (right side)—well beyond the stage I mode-beating oscillations. The resulting spectra are dominantly single quasimonoenergetic peaks. By restricting the dopant gas region, we have limited the number of electron injection events from longitudinal oscillations in pulse intensity. This is reproduced in the simulation [Figs. 4(d) and 4(e)]. The narrowest peaks in Fig. 4 show energy spreads of <10%.

To summarize, we have presented experiments and simulations showing that a universal mode-beating effect in meter-scale low density plasma waveguides—*occurring whether or not the injected laser is linearly mode-matched*—enhances ionization injection to produce multipeak, multi-GeV electron spectra or single quasimonoenergetic peaks. Enhancement occurs mainly due to mode-beating-driven back-and-forth oscillations in peak a_0. Additional spectrum control may be possible using waveguide sections with much higher dopant concentration. For example, Fig. 4(c) shows a spectrum where the dopant gas mix, at $z = 14$ cm, was replaced with pure N_2 gas, producing a continuous spectrum with a peak at ∼1.3 GeV in a narrow, ∼milliradian angular beam profile. Because the Bessel-beam-induced shock expansion in nitrogen is significantly slower than for hydrogen, the index structure in the injector section is narrowed. The guided pulse is then squeezed into a smaller channel at the injection section, increasing the pulse intensity above the ionization injection threshold and promoting continuous ionization injection. Across all of our experimental conditions, such continuous spectra were generated only with the use of a pure N_2 injector, which suggests the possibility of electron spectrum control by guided mode shaping.

Acknowledgments—The authors thank Mayank Gupta for lab assistance, Scott Wilks for technical discussions, and Revathi Jambunathan and Jean-Luc Vay for help with WarpX [20], an open-source particle-in-cell code used for simulations in this Letter. This work was supported by the U.S. DOE (DE-SC0015516, LaserNetUS DE-SC0019076/FWP#SCW1668, and DE-SC0011375), NSF (PHY2010511), and the Defense Advanced Research Projects Agency (DARPA) under the Muons for Science and Security Program. Simulations used DOD high performance computing support provided through ONR (N00014-20-1-2233) and AFOSR (FA9550-21-1-0405). WarpX [38] is primarily funded by the US DOE Exascale Computing Project, with contributors at LBNL, LLNL, CEA-LIDYL, SLAC, DESY, CERN, and TAE Technologies. J. J. R. acknowledges support of ONR (N000142012842). A. J. G. and A. P. are supported by supported by the U.S. DOE (DE-AC02-05CH11231). E. R. is supported by an NSF Graduate Research Fellowship (DGE 1840340).

[1] E. Esarey, C. B. Schroeder, and W. P. Leemans, Physics of laser-driven plasma-based electron accelerators, Rev. Mod. Phys. **81**, 1229 (2009).

[2] E. Esarey, P. Sprangle, J. Krall, and A. Ting, Overview of plasma-based accelerator concepts, IEEE Trans. Plasma Sci. **24**, 252 (1996).

[3] X. Wang *et al.*, Quasi-monoenergetic laser-plasma acceleration of electrons to 2 GeV, Nat. Commun. **4**, 1988 (2013).

[4] H. T. Kim, K. H. Pae, H. J. Cha, I. J. Kim, T. J. Yu, J. H. Sung, S. K. Lee, T. M. Jeong, and J. Lee, Enhancement of electron energy to the multi-GeV regime by a dual-stage laser-wakefield accelerator pumped by petawatt laser pulses, Phys. Rev. Lett. **111**, 165002 (2013).

[5] A. J. Gonsalves *et al.*, Petawatt laser guiding and electron beam acceleration to 8 GeV in a laser-heated capillary discharge waveguide, Phys. Rev. Lett. **122**, 084801 (2019).

[6] B. Miao, J. E. Shrock, L. Feder, R. C. Hollinger, J. Morrison, R. Nedbailo, A. Picksley, H. Song, S. Wang, J. J. Rocca, and H. M. Milchberg, Multi-GeV electron bunches from an all-optical laser wakefield accelerator, Phys. Rev. X **12**, 031038 (2022).

[7] C. G. Durfee and H. M. Milchberg, Light pipe for high intensity laser pulses, Phys. Rev. Lett. **71**, 2409 (1993).

[8] C. G. Durfee, J. Lynch, and H. M. Milchberg, Development of a plasma waveguide for high-intensity laser pulses, Phys. Rev. E **51**, 2368 (1995).

[9] T. R. Clark and H. M. Milchberg, Optical mode structure of the plasma waveguide, Phys. Rev. E **61**, 1954 (2000).

[10] Y. Ehrlich, C. Cohen, A. Zigler, J. Krall, P. Sprangle, and E. Esarey, Guiding of high intensity laser pulses in straight and curved plasma channel experiments, Phys. Rev. Lett. **77**, 4186 (1996).

[11] A. Butler, D. J. Spence, and S. M. Hooker, Guiding of high-intensity laser pulses with a hydrogen-filled capillary discharge waveguide, Phys. Rev. Lett. **89**, 185003 (2002).

[12] N. Lemos, T. Grismayer, L. Cardoso, G. Figueira, R. Issac, D. A. Jaroszynski, and J. M. Dias, Plasma expansion into a waveguide created by a linearly polarized femtosecond laser pulse, Phys. Plasmas **20**, 063102 (2013).

[13] N. Lemos, L. Cardoso, J. Geada, G. Figueira, F. Albert, and J. M. Dias, Guiding of laser pulses in plasma waveguides created by linearly-polarized femtosecond laser pulses, Sci. Rep. **8**, 3165 (2018).

[14] R. J. Shalloo, C. Arran, L. Corner, J. Holloway, J. Jonnerby, R. Walczak, H. M. Milchberg, and S. M. Hooker, Hydrodynamic optical-field-ionized plasma channels, Phys. Rev. E **97**, 053203 (2018).

[15] R. J. Shalloo, C. Arran, A. Picksley, A. von Boetticher, L. Corner, J. Holloway, G. Hine, J. Jonnerby, H. M. Milchberg, C. Thornton, R. Walczak, and S. M. Hooker, Low-density hydrodynamic optical-field-ionized plasma channels generated with an axicon lens, Phys. Rev. Accel. Beams **22**, 041302 (2019).

[16] S. Smartsev, C. Caizergues, K. Oubrerie, J. Gautier, J.-P. Goddet, A. Tafzi, K. T. Phuoc, V. Malka, and C. Thaury, Axiparabola: A long-focal-depth, high-resolution mirror for broadband high-intensity lasers, Opt. Lett. **44**, 3414 (2019).

[17] A. Picksley, A. Alejo, J. Cowley, N. Bourgeois, L. Corner, L. Feder, J. Holloway, H. Jones, J. Jonnerby, H. M. Milchberg, L. R. Reid, A. J. Ross, R. Walczak, and S. M. Hooker, Guiding of high-intensity laser pulses in 100-mm-long hydrodynamic optical-field-ionized plasma channels, Phys. Rev. Accel. Beams **23**, 081303 (2020).

[18] A. Picksley, A. Alejo, R. J. Shalloo, C. Arran, A. von Boetticher, L. Corner *et al.*, Meter-scale conditioned hydrodynamic optical-field-ionized plasma channels, Phys. Rev. E **102**, 053201 (2020).

[19] B. Miao, L. Feder, J. E. Shrock, A. Goffin, and H. M. Milchberg, Optical guiding in meter-scale plasma waveguides, Phys. Rev. Lett. **125**, 074801 (2020).

[20] L. Feder, B. Miao, J. E. Shrock, A. Goffin, and H. M. Milchberg, Self-waveguiding of relativistic laser pulses in neutral gas channels, Phys. Rev. Res. **2**, 043173 (2020).

[21] A. Morozov, A. Goltsov, Q. Chen, M. Scully, and S. Suckewer, Ionization assisted self-guiding of femtosecond laser pulses, Phys. Plasmas **25**, 053110 (2018).

[22] J. E. Shrock, B. Miao, L. Feder, and H. M. Milchberg, Meter-scale plasma waveguides for multi- GeV laser wakefield acceleration, Phys. Plasmas **29**, 073101 (2022).

[23] T. P. Rowlands-Rees, C. Kamperidis, S. Kneip, A. J. Gonsalves, S. P. D. Mangles *et al.*, Laser-driven acceleration of electrons in a partially ionized plasma channel, Phys. Rev. Lett. **100**, 105005 (2008).

[24] A. Pak, K. A. Marsh, S. F. Martins, W. Lu, W. B. Mori, and C. Joshi, Injection and trapping of tunnel-ionized electrons into laser-produced wakes, Phys. Rev. Lett. **104**, 025003 (2010).

[25] C. McGuffey, A. G. R. Thomas, W. Schumaker, T. Matsuoka, V. Chvykov, F. J. Dollar, G. Kalintchenko, V. Yanovsky, A. Maksimchuk, K. Krushelnick, V. Y. Bychenkov, I. V. Glazyrin, and A. V. Karpeev, Ionization induced trapping in a laser wakefield accelerator, Phys. Rev. Lett. **104**, 025004 (2010).

[26] C. E. Clayton, J. E. Ralph, F. Albert, R. A. Fonseca, S. H. Glenzer, C. Joshi, W. Lu, K. A. Marsh, S. F. Martins, W. B. Mori, A. Pak, F. S. Tsung, B. B. Pollock, J. S. Ross, L. O. Silva, and D. H. Froula, Self-guided laser wakefield acceleration beyond 1 GeV using ionization-induced injection, Phys. Rev. Lett. **105**, 105003 (2010).

[27] J. L. Vay *et al.*, Modeling a chain of three plasma accelerator stages with the WarpX electromagnetic PIC code on GPUs, Phys. Plasmas **28**, 023105 (2021).

[28] See Supplemental Material at http://link.aps.org/supplemental/10.1103/PhysRevLett.133.045002 for linear mode analysis of plasma waveguides, additional PIC simulations, movies of pulse propagation, and a simple model of mode beating in ponderomotively modified waveguides.

[29] T. R. Clark and H. M. Milchberg, Frequency selective tunnel coupling to the plasma fiber, Phys. Rev. Lett. **81**, 357 (1998).

[30] P. Sprangle, E. Esarey, J. Krall, and G. Joyce, Propagation and guiding of intense laser pulses in plasmas, Phys. Rev. Lett. **69**, 2200 (1992).

[31] C. B. Schroeder, C. Benedetti, E. Esarey, J. van Tilborg, and W. P. Leemans, Group velocity and pulse lengthening of mismatched laser pulses in plasma channels, Phys. Plasmas **18**, 083103 (2011).

[32] C. Benedetti, C. B. Schroeder, E. Esarey, and W. P. Leemans, Quasi-matched propagation of ultra-short, intense

laser pulses in plasma channels, Phys. Plasmas **19**, 053101 (2012).
[33] C. Benedetti, F. Rossi, C. B. Schroeder, E. Esarey, and W. P. Leemans, Pulse evolution and plasma-wave phase velocity in channel-guided laser-plasma accelerators, Phys. Rev. E **92**, 023109 (2015).
[34] B. A. Shadwick, C. B. Schroeder, and E. Esarey, Nonlinear laser energy depletion in laser-plasma accelerators, Phys. Plasmas **16**, 056704 (2009).
[35] Y. Wang, S. Wang, A. Rockwood, B. M. Luther, R. Hollinger, A. Curtis, C. Calvi, C. S. Menoni, and J. J. Rocca, 0.85 PW laser operation at 3.3 Hz and second-harmonic beamline, Opt. Lett. **42**, 3828 (2017).
[36] A. J. Gonsalves *et al.*, Laser-heated capillary discharge plasma waveguides for electron acceleration to 8 GeV, Phys. Plasmas **27**, 053102 (2020).
[37] A. J. Gonsalves *et al.*, Tunable laser plasma accelerator based on longitudinal density tailoring, Nat. Phys. **7**, 862 (2011).
[38] https://github.com/ECP-WarpX/WarpX.
[39] B. Miao, L. Feder, J. E. Shrock, and H. M. Milchberg, Phase front retrieval and correction of Bessel beams, Opt. Express **30**, 11360 (2022).
[40] D. F. Gordon, A. Ting, T. Jones, B. Hafizi, R. F. Hubbard, and P. Sprangle, Particle-in-cell simulations of optical injectors for plasma accelerators, Proc. IEEE Part. Accel. Conf. **3**, 1846 (2003), https://ieeexplore.ieee.org/stamp/stamp.jsp?arnumber=1288824.
[41] A. Buck, K. Zeil, A. Popp, K. Schmid, A. Jochmann, S. D. Kraft, B. Hidding, T. Kudyakov, C. M. S. Sears, L. Veisz, S. Karsch, J. Pawelke, R. Sauerbrey, T. Cowan, F. Krausz, and U. Schramm, Absolute charge calibration of scintillating screens for relativistic electron detection, Rev. Sci. Instrum. **81**, 033301 (2010).
[42] T. Kurz, J. P. Couperus, J. M. Krämer, H. Ding, S. Kuschel, A. Köhler, O. Zarini, D. Hollatz, D. Schinkel, R. D'Arcy, J.-P. Schwinkendorf, J. Osterhoff, A. Irman, U. Schramm, and S. Karsch, Calibration and cross-laboratory implementation of scintillating screens for electron bunch charge determination, Rev. Sci. Instrum. **89**, 093303 (2018).
[43] R. Lehe, M. Kirchen, I. A. Andriyash, B. B. Godfrey, and J.-L. Vay, A spectral, quasi-cylindrical and dispersion-free particle-in-cell algorithm, Comput. Phys. Commun. **203**, 66 (2016).
[44] R. Lehe, Improvement of laser-wakefield accelerators: Towards a compact free electron laser, Ph.D. thesis, Ecole Polytechnique (2014), https://pastel.hal.science/tel-01088398/document.

End Matter

Appendix A: Experimental setup—Figure 5(a) is a sketch of the experimental configuration. Plasma waveguides were generated by initial Bessel beam heating, via optical-field ionization, of a 20 cm long multi-valve-fed gas jet followed by self-waveguiding of the main end-injected pulse [20], which also drives LWFA. We used three gas flow configurations in our experiments: pure H_2 in all valves, a dopant gas mix (95%/5%$-H_2/N_2$) in all valves, or pure H_2 in all valves with added localized injection of the dopant gas mix. Figure 5(b) plots longitudinal atomic hydrogen gas density profiles [22] used in the experiments. The axial nonuniformity originates from the six discrete gas supply valves and slight machining variations in the jet throat. Further details on diagnostics of the gas jet and plasma waveguide and on phase front correction of Bessel beams are found in [6,22,39]. The ability of the injector to axially localize the dopant gas is demonstrated in Fig. 5(c). The jet was first run with H_2 in the six valves and pure N_2 in the injector valve, with the fluorescence image collected through an interference filter passing only the H-α emission. The blue curve is the extracted axial density profile of atomic hydrogen, showing a notch at the location of the injector. Then the gases were switched, with H_2 in the injector and N_2 in the six valves, yielding the orange curve showing the axial specificity of injection. As in Refs. [6,22], the permanent magnet electron spectrometer is located outside the vacuum chamber, requiring propagation of the electron beam through an aluminum flange prior to dispersion in the

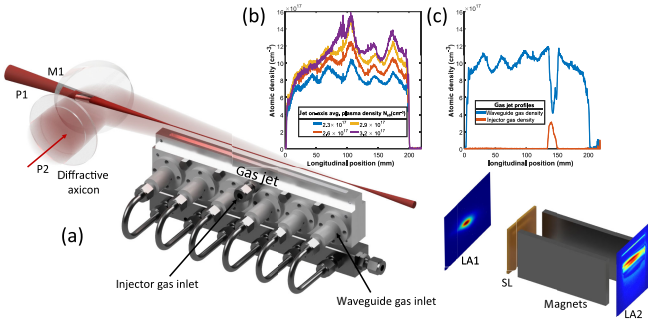

FIG. 5. (a) Sketch of experiment. A 10–15 J 45–65 fs, $w_0 =$ 30 μm drive pulse (P1) is focused into the prepared index structure formed 2.5 ns after an initial plasma column has been generated by a synchronized 0.5 J, 75 fs zeroth-order Bessel beam (J_0) pulse (P2) with a ~40 cm long central focal line 3 mm above a 20 cm supersonic (Mach 4) H_2 gas jet. The J_0 pulse is produced by splitting a portion of the main beam, compressing it in a separate compressor, and focusing it with a diffractive axicon. The jet is supplied by six gas valves and has localized inlets for dopant gas to seed ionization injection. Accelerated electron bunches exit the end of the waveguide and pass through an 0.85 mm thick aluminum exit flange and LANEX screen (LA1) [41,42] before entering a 0.93 T permanent magnet spectrometer with an adjustable 0.25–1 mm collimating slit (SL). The dispersed electron spectrum is recorded on LANEX (LA2), and imaged with an Andor Zyla 4.2 camera. (b) Atomic hydrogen density profiles and associated on-axis waveguide plasma densities. (c) Example of gas distributions with use of a localized N_2 injector at $z = 14$ cm from the waveguide entrance.

magnetic field. Ray tracing simulations [40] suggest that this increases the apparent energy spread and divergence of dispersed electron beams.

Appendix B: Correlation of ionization injection and mode beating—To investigate the effect of mode beating on electron injection, we performed a quasi-3D simulation with FBPIC (Fourier-Bessel particle-in-cell code) [43], employing particle tracking, for the same parameters as for the blue curve in Fig. 1(a). Here, particles >50 MeV in the bunch at $z = 10$ cm are tracked back to their z location of birth. The simulation was performed in a boosted frame with $\gamma = 2$, with four azimuthal modes and eight tracked particles per cell (eight per azimuthal, one per radial, and one per longitudinal grid segment). The field and tracked particle data were saved every 20 μm from $z = 0$ to z = 10 cm. Electrons born slightly after a save location may evolve over several simulation steps before being recorded as "new" particles at the next save location.

Figure 6(a) plots the on-axis laser envelope in (ξ, z) space along with the charge per unit length dQ/dz injected vs z (white curve). The overall rise of the white curve (apart from its modulations) occurs as the laser peak intensity position retreats in the light frame, leading to slower wake velocity and enhanced charge injection. The evident correlation between envelope oscillation and injection in Fig. 6(a) is explained by Fig. 6(b), which replots dQ/dz (blue curve) along with the relative wake position $\Delta\xi_{\mathrm{wake}} = \xi_{\mathrm{wake}} - \langle\xi_{\mathrm{wake}}\rangle_{1\ \mathrm{cm}}$ (purple curve), relative position of a_0 peak $\Delta\xi_{a_0,\mathrm{peak}} = \xi_{a_0,\mathrm{peak}} - \langle\xi_{a_0,\mathrm{peak}}\rangle_{1\ \mathrm{cm}}$ (red curve), and peak a_0 vs z (green curve). The wake position ξ_{wake} is the location where $E_z = 0$, the potential minimum or trapping center near the back of the wake bubble, and $\langle\,\rangle_{1\ \mathrm{cm}}$ denotes an average over 1 cm of propagation. Note that few electrons injected in the early part of the waveguide ($z < \sim$25 mm) survive to $z = 100$ mm; the injected electrons are dominantly from stage II of propagation. Figure 6(c) plots the laser field envelope (top half of frame) and plasma density (bottom half) overlaid with injected electron initial locations (white dots and circles) during a full cycle of beating. Given the 20 μm save interval for the simulation, electrons born slightly after a save location may evolve over several simulation steps before being recorded as "new" particles at the next save location. This is why the axial extent of the white circles in Fig. 6(c) is approximately 20 μm, with those on the left closest to trapping. The white dots to the right mark likely birth locations of trapped electrons in a given frame.

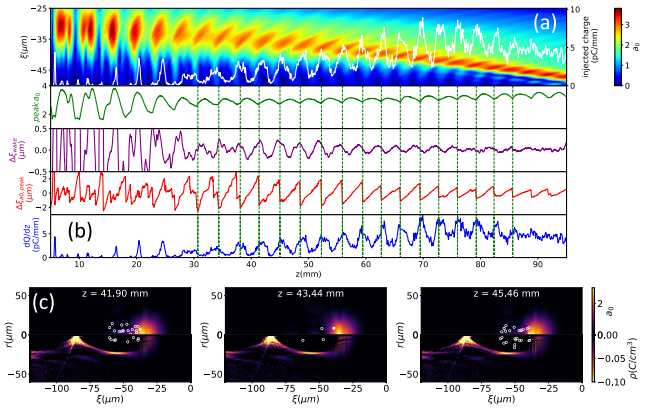

FIG. 6. FBPIC simulation with particle tracking, for the same parameters as the blue curve of Fig. 1(a). (a) On-axis evolution of the laser envelope (a_0) in the light frame (computation window, $\xi = z - v_g t$), showing the periodic motion of the laser pulse peak and pulse retreat in the light frame. The white curve is a histogram of electron injection locations contributing to the bunch at $z = 10$ cm with electrons >50 MeV. (b) Lineouts of pulse and wake parameters vs propagation distance (see text). Green curve: peak a_0 in moving window. Purple curve: relative position of the back of the wake, $\Delta\xi_{\mathrm{wake}} = \xi_{\mathrm{wake}} - \langle\xi_{\mathrm{wake}}\rangle_{1\ \mathrm{cm}}$. Red curve: relative position of peak a_0, $\Delta\xi_{a_0,\mathrm{peak}} = \xi_{a_0,\mathrm{peak}} - \langle\xi_{a_0,\mathrm{peak}}\rangle_{1\ \mathrm{cm}}$. Blue curve: replot of white curve from panel (a). (c) Laser field envelope (top half of frame) and plasma density (bottom half) overlaid with injected electron initial locations (white dots and circles) over a full cycle of beating, showing two injection maxima and a minimum. The dots mark likely birth locations of trapped electrons in a given frame.

Figure 6 makes clear that injection is enhanced when mode beating shifts the location of maximum a_0 closest to the wake trapping center; for this phase of the beating, peak a_0 in the moving frame is a minimum. During stage II, the oscillations of $\Delta\xi_{a_0,\mathrm{peak}}$ are an order of magnitude larger than $\Delta\xi_{\mathrm{wake}}$, showing that periodically enhanced injection is mainly due to the mode-beating-driven back-and-forth oscillations in peak a_0, and not oscillations in wake velocity as may occur under other conditions [33,44].